The Astrophysical Journal, 994:197 (10pp), 2025 December 1 https://doi.org/10.3847/1538-4357/ae11aa

H I 21 cm Absorption Associated with Foreground Galaxies on Top of Quasars

Labanya K. Guha[1], Raghunathan Srianand[2], and Rajeshwari Dutta[2]
[1] Indian Institute of Astrophysics (IIA), Koramangala, Bangalore 560034, India; labanya.guha@iiap.res.in
[2] IUCAA, Postbag 4, Ganeshkhind, Pune 411007, Maharashtra, India
Received 2025 March 24; revised 2025 October 7; accepted 2025 October 8; published 2025 November 26

Abstract

A systematic search for H I 21 cm absorption in quasar–galaxy pairs (QGPs) provides a powerful means to map the distribution of cold gas around high-redshift star-forming galaxies. Fiber spectroscopy of high-redshift quasars enables the serendipitous detection of foreground star-forming galaxies at extremely small impact parameters, forming a unique subset of QGPs known as galaxies on top of quasars (GOTOQs). In this study, we present results from a pilot upgraded Giant Metrewave Radio Telescope survey of three GOTOQs, where we achieved a remarkable 100% detection rate of H I 21 cm absorption. By combining our findings with the existing literature, we establish that GOTOQs constitute a distinct population in terms of H I 21 cm absorption, with significantly higher detection rates than those observed in damped Lyα-based or metal absorption-based searches. For the GOTOQs, we find a strong correlation between the line-of-sight reddening and the H I 21 cm optical depth, characterized by $\int \tau\, dv\ (\mathrm{km\ s^{-1}}) = 13.58^{+2.75}_{-2.35}E(B-V) + 0.68^{+1.06}_{-1.27}$, consistent with the Milky Way sightlines. We also show that the H I 21 cm optical depth declines with the impact parameter, and find a tentative trend for the H I 21 cm detection rates to also decline with the impact parameter. With upcoming wide-field spectroscopic surveys expected to substantially expand the catalog of known GOTOQs, the success of this pilot survey lays the foundation for constructing a statistically significant sample of intervening H I 21 cm absorbers.

Unified Astronomy Thesaurus concepts: Quasar absorption line spectroscopy (1317); Circumgalactic medium (1879)

1. Introduction

Galaxy evolution is believed to be governed by the slowly varying equilibrium between the gas inflows from the intergalactic medium (IGM), gas outflows from the galaxy to the circumgalactic medium (CGM) and the IGM, and in situ star formation occurring within the galaxy (D. K. Erb 2008; R. C. Kennicutt & N. J. Evans 2012; J. Tumlinson et al. 2013; C. Péroux et al. 2020). Obtaining direct constraints on the gas inflow and outflow rates and how they evolve with redshift (i.e., cosmic time) is crucial for our understanding of galaxy evolution. In particular, H I 21 cm absorption detected toward radio-loud sources is useful in probing the properties of cold neutral gas in and around galaxies and their redshift evolution.

The H I 21 cm absorption serves as a powerful diagnostic tool for probing various physical properties of the neutral gas. It provides key insights into (1) the parsec-scale structure of the H I gas through Very Long Baseline Interferometry (VLBI) observations (R. Srianand et al. 2013); (2) the thermal state of the H I gas (C. Heiles & T. H. Troland 2003) as the spin temperature (T_s) of neutral hydrogen, which governs the relative population of the hyperfine levels responsible for the 21 cm line, is influenced by the kinetic temperature (T_k) of the gas through collisional interactions and resonant scattering of Lyα photons (G. B. Field 1959; H. Liszt 2001; N. Roy et al. 2006); (3) the presence and strength of magnetic fields in the interstellar medium (ISM) via Zeeman splitting (C. Heiles & T. H. Troland 2004); and (4) the filling factor of cold gas in both the ISM and the CGM.

Most of the detections of H I 21 cm absorption at $z < 1.5$ to date are based on searches toward strong Mg II absorbers (e.g., F. H. Briggs & A. M. Wolfe 1983; N. Gupta et al. 2009; N. Kanekar et al. 2009; R. Dutta et al. 2017a). Based on these studies, the average detection rate of H I 21 cm absorption in samples of strong Mg II systems (defined as rest equivalent width of the Mg II λ2796 line, $W_{2796} \geqslant 1$ Å) is found to be ~10%–20% for an optical depth sensitivity of $\int \tau dv = 0.3\ \mathrm{km\ s^{-1}}$. This incidence is found to remain constant, within the measurement uncertainties, over the redshift range $z \simeq 0.3$–1.5 (R. Dutta et al. 2017a). Further, the H I 21 cm absorption detection rate is shown to increase (i) with the equivalent width of Mg II and Fe II (R. Dutta et al. 2017b), (ii) with higher cut-offs in the equivalent width ratio of Mg I/Mg II and Mg II/Fe II (N. Gupta et al. 2012), and (iii) when the background quasar is dust reddened (C. L. Carilli et al. 1998; R. Dutta et al. 2020a). Typically, associated galaxies are found within ≈30 kpc of the lines of sight (see, for example, the compilation of S. J. Curran et al. 2016; R. Dutta et al. 2017c). However, due to various biases associated with the optical preselection and lack of independent H I column density measurements in most cases, interpreting the detection rate of H I 21 cm absorption from such an "absorber-centric" sample is not straightforward.

To effectively map the distribution and the redshift evolution of the H I 21 cm absorbers, conducting a blind survey of H I 21 cm absorbers is thus essential. This has recently become possible thanks to the advent of sensitive, wide-band receivers on radio interferometers. N. Gupta et al. (2021) carried out a blind survey (covering a redshift path length of ~13 at $z \sim 0.18$) with the upgraded Giant Metrewave Radio Telescope (uGMRT; Y. Gupta et al. 2017), and placed a constraint on the number of H I 21 cm absorbers per unit redshift of $\leqslant 0.14$ for $\int \tau dv \geqslant 0.3\ \mathrm{km\ s^{-1}}$, corresponding to H I column density, $N_{\mathrm{HI}} \gtrsim 5 \times 10^{19}\ \mathrm{cm^{-2}}$ for $T_s = 100$ K. Using

the position of nearby photometric galaxies, they also concluded that the covering factor of H I gas is $\leqslant$0.022 for the impact parameters (D)[3] in the range 50 kpc $\leqslant D \leqslant$ 150 kpc. E. M. Sadler et al. (2020) have detected 4 H I 21 cm absorbers in their blind survey using Australian Square Kilometer Array Pathfinder (ASKAP; A. W. Hotan et al. 2021) covering the redshift path length of 21.37 (at a median $z \sim 0.6$) for detecting typical damped Lyα absorbers (DLAs) with spin temperature of 100 K. This provided the number of absorbers per unit redshift path of $0.19^{+0.15}_{-0.09}$. In the future, full survey data releases from ongoing blind surveys with ASKAP (J. R. Allison et al. 2022) and MeerKAT (N. Gupta 2015) will provide unbiased statistics on the redshift distribution of H I 21 cm absorbers at $z \leqslant 1.5$.

However, it is important to keep in mind that purely based on geometric considerations, blind surveys are likely to yield a limited number of background sightlines that pass through the halos of foreground galaxies at low impact parameters. Therefore, complementary to absorber-centric searches, several studies have used close projected pairs of background quasars and foreground galaxies, known as quasar–galaxy pairs (QGPs), to map the distribution of cold atomic gas around low-redshift ($z < 0.4$) galaxies (C. L. Carilli & J. H. van Gorkom 1992; N. Gupta et al. 2010; S. Borthakur et al. 2011; M. A. Zwaan et al. 2015; S. N. Reeves et al. 2016; R. Dutta et al. 2017c). However, H I 21 cm emission studies have shown that high-column-density H I gas ($N_{\rm H\,I} \gtrsim 10^{20}$ cm^{-2}) is typically confined to within $\approx$2–3 times the optical radius of isolated galaxies (J. A. Irwin 1995; M. A. Zwaan et al. 2005; S. N. Reeves et al. 2015). Consequently, targeted "galaxy-centric" surveys focusing on galaxies at low impact parameters (i.e., within a few optical radii) are essential for probing the distribution of cold gas. Furthermore, observations indicate that the detection rate of H I 21 cm absorption is highest at such low impact parameters, with the covering fraction of cold neutral gas reaching $\approx$24% at $D \leqslant$ 15 kpc (R. Dutta et al. 2017c), implying the importance of these focused surveys.

Here, we design an experiment to probe the cold H I gas close to galaxies using fiber-fed spectroscopic observation, which is expected to capture photons from all objects present within the projected area of the fiber in addition to the photons from the primary target. For example, the Sloan Digital Sky Survey (SDSS; D. G. York et al. 2000) spectroscopy of a distant quasar can detect nebular emission lines from foreground galaxies typically within $D \sim 2$ kpc at redshift $z \sim 0.1$ and $\sim$10 kpc at $z \sim 1$. D. G. York et al. (2012) named such galaxies as galaxies on top of quasars (GOTOQs; see also P. Noterdaeme et al. 2010; L. A. Straka et al. 2013, 2015; R. Joshi et al. 2017, 2018; K. H. R. Rubin et al. 2022; S. Das et al. 2025). GOTOQs thus provide excellent targets to probe the cold H I gas at low impact parameters to star-forming galaxies over a wide range of redshifts. This forms the main motivation of this pilot survey.

This paper is organized as follows. In Section 2, we provide the basic details of our sample. Details of our uGMRT observations and data reduction are provided in Section 3. Analysis and results are summarized in Section 4. Section 5 discusses and summarizes the main results of our paper. Throughout this work, we use flat ΛCDM cosmology with $\Omega_\Lambda = 0.7$, $\Omega_m = 0.3$, and $H_0 = 70$ km s^{-1} Mpc^{-1}.

[3] Impact parameter (D) is the projected separation between the center of the galaxy and the background line of sight.

2. Sample

The GOTOQs searched for H I 21 cm absorption in this work are drawn from a parent sample constructed by L. K. Guha et al. (2025, in preparation). This parent sample, the largest of its kind to date, consists of about 500 GOTOQs at $z_{\rm GOTOQ} < 0.4$ from SDSS-DR16 (S. Alam et al. 2015). Briefly, GOTOQs are identified from quasar spectra using the following procedure: the continuum is first subtracted using `QSmooth` (D. Ďurovčíková et al. 2020), and the regions around prominent quasar emission lines are masked. The continuum-subtracted spectrum is then smoothed over three pixels to search for possible foreground galaxy emission lines. A peak-finding algorithm detects the emission features, which are then matched to appropriately redshifted known nebular emission lines. Spectra with at least three matching lines detected with a significance of at least 3σ are marked as potential candidate GOTOQs and are finally visually inspected to confirm them as GOTOQs.

To identify associated H I 21 cm absorption in GOTOQs, we cross-matched the GOTOQs with the Faint Images of the Radio Sky at Twenty-Centimeters 1.4 GHz (R. L. White et al. 1997) and Very Large Array Sky Survey 3 GHz (Y. A. Gordon et al. 2021) radio source catalogs. We selected sources with a peak flux density exceeding 30 mJy and ensured that the expected H I 21 cm signal was free from contamination by known strong Radio Frequency Interference (RFI) at uGMRT. The cross-matching criterion required the optical and radio centroids of the quasars to be within 1″ of each other. This process identified seven GOTOQs, one of which has been previously observed in the literature (S. Borthakur et al. 2010). We are conducting a systematic search for cold gas in the remaining systems, with observations of four quasars completed using uGMRT in cycle 46. Details of these observed GOTOQs are provided in Table 1. The observations of one of these four systems (i.e., J0055+1408) are severely affected by scintillation, resulting in data that are inadequate for analysis. Consequently, this system is excluded from the study, and we focus on presenting observations for the remaining three systems.

Available optical data for these three GOTOQs are shown in Figure 1. Each horizontal panel in this figure consists of two plots: the left plot displays the nebular emission lines detected in the continuum-subtracted SDSS quasar spectrum. The prominent nebular emission lines from the foreground galaxy are marked by red dashed vertical lines, and the fit to the data is shown in blue. The [O II] $\lambda\lambda$ 3727, 3729 emission doublets are fitted with double Gaussians, with both lines having the same redshift and velocity widths, while other nebular emission lines are fitted using a single Gaussian. The plot on the right shows a composite *griz* band Dark Energy Survey Instrument—Legacy Imaging Survey (DESI-LIS; A. Dey et al. 2019) image of the quasar field, with the quasar marked by a red star and the area covered by the observing fiber outlined by a blue circle. The foreground galaxy is clearly visible in only one case (i.e., J1451+0857), where we could measure the impact parameter. In the other two cases, we could get only an upper limit on the impact parameter based on the SDSS or Baryon Oscillation Spectroscopic Survey (BOSS) fiber sizes.

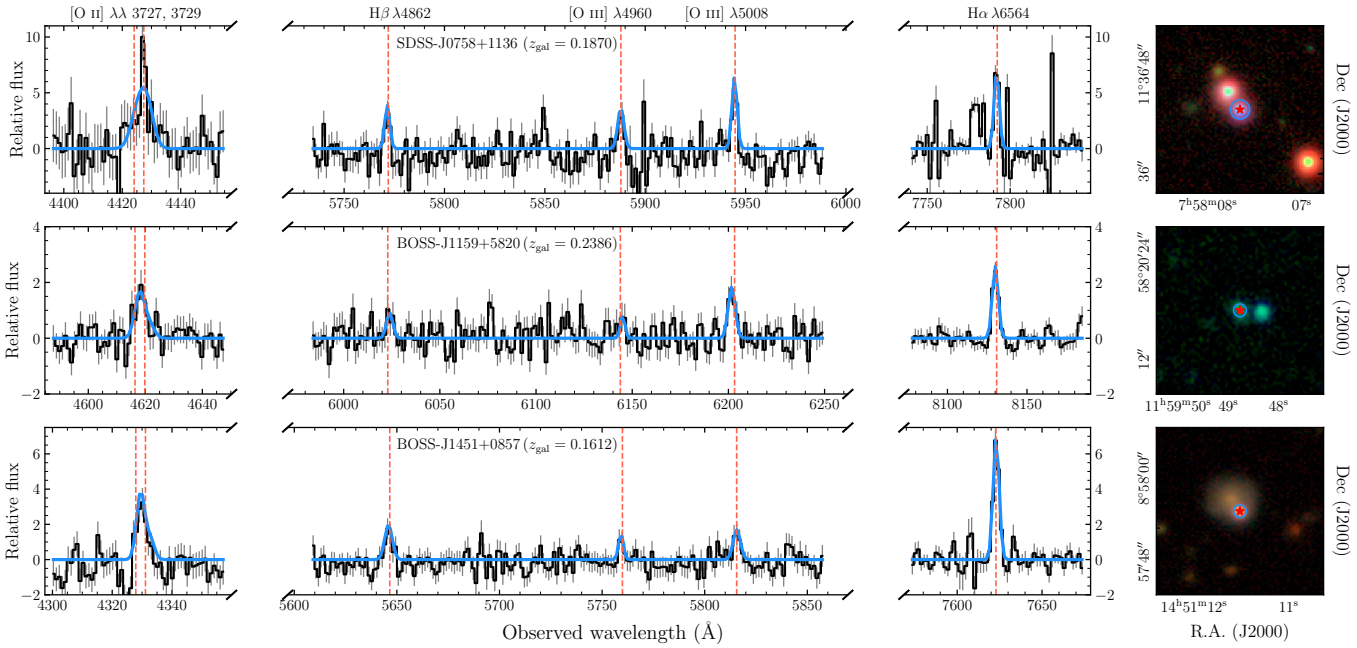

Figure 1. Optical properties of GOTOQs observed with the uGMRT. Each horizontal panel consists of two plots: the left plot displays the nebular emissions detected in the continuum-subtracted SDSS/eBOSS quasar spectrum, where the prominent nebular emission lines from the foreground galaxy are marked by red dashed vertical lines, and the fit to the data is shown in blue. The right plot shows a composite *griz* band DESI-LIS image of the quasar field, with the quasar marked by a red star and the observing fiber outlined by a blue circle. Flux scales in the left panels are in the units of 10^{-17} erg s^{-1} cm^{-2} Å^{-1}.

Table 1
Log of Our uGMRT Observations

(1) GOTOQ	(2) z_{QSO}	(3) z_{gal}	(4) Observation Date	(5) On-source Time (minutes)	(6) δv_{ch} (km s^{-1})	(7) rms Noise (mJy beam^{-1})	(8) f_{peak} (mJy beam^{-1})
J005503.52+140806.50*	1.666	0.2015	2024 Nov 30	111	…	…	…
J075807.65+113646.00	0.569	0.1870	2024 Nov 15	64	0.76	5.4	420
J115948.76+582020.00	1.280	0.2386	2024 Jul 19	12	0.80	13.1	1389
J145111.51+085757.80	1.355	0.1612	2024 Jul 19	234	0.75	3.0	36

Note. Columns (1), (2), and (3) provide the GOTOQs system name, redshift of the background quasars, and the redshift of the foreground galaxies, respectively. Columns (4) and (5) provide the date of observations and the on-source observing time for the targets, respectively. Columns (6) and (7), respectively, indicate the channel width in the velocity space and the rms noise of the spectrum. Column (8) lists the peak radio flux density of the background quasar in the uGMRT image. Observations of the system marked with a ⋆, J0055+1408, are severely affected by scintillations.

3. Observations and Data Reduction

The sample was observed using Band 5 of uGMRT between 2024 July and December (Proposal ID: 46_058). The sources were observed for ≈1–6 hr depending on their radio continuum flux density, to reach a similar optical depth sensitivity (see Table 1). Standard flux density and gain calibrators were observed in regular intervals during the course of the observations. The data were obtained in two parallel hand correlations. The spectral setup used a bandwidth of 6.25 MHz split into 2048 channels, giving a channel width of 3 kHz. The data reduction was carried out using the Common Astronomy Software Package (CASA, version 6.6; J. P. McMullin et al. 2007), and involved standard procedures of data editing, gain and bandpass calibration, and iterative cycles of self-calibration and imaging. In addition to manual data editing in CASA, the AOFLAGGER package (A. R. Offringa et al. 2012) was used to flag data affected by RFI. After subtracting the continuum emission from the self-calibrated visibilities, the spectral cubes were obtained using Briggs robust = 0 weighting. The typical angular resolution of the cubes and continuum images for this weighting scheme is ≈2″–3″. The radio contours overlayed on the optical images are shown in Appendix A. The H I 21 cm absorption spectra were extracted toward the peak of the continuum flux density of the radio sources. If required, a low-order polynomial was fit to the line-free channels of the spectra to remove any residual continuum emission.

4. Analysis and Results

We detect H I 21 cm absorption toward the background radio-loud quasars associated with all three GOTOQs for which we could secure reliable spectra with uGMRT. Figure 2 provides the H I 21 cm absorption spectra for these GOTOQs: J0758+1136 (left panel), J1159+5820 (middle panel), and J1451+0857 (right panel). The continuum-normalized observed spectra are plotted in black, while the overall multiple-component Gaussian fits to the absorption profiles are shown in red. The individual Gaussian components are shown using blue dashed lines. The full width at half-maximum (FWHM) of individual Gaussian components

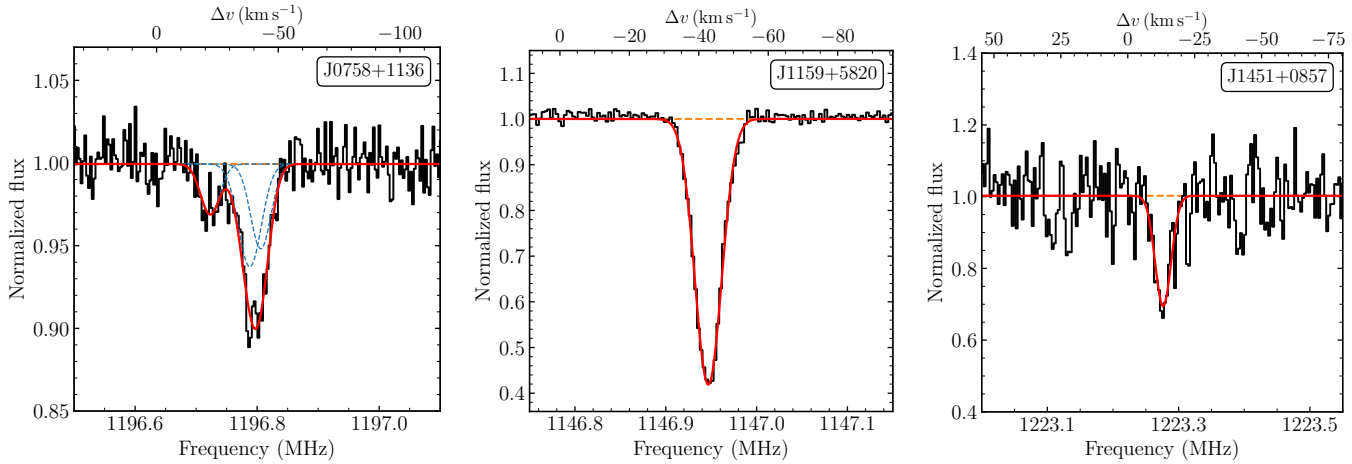

Figure 2. H I 21 cm absorption spectra of three GOTOQs: J0758+1136 (left panel), J1159+5820 (middle panel), and J1451+0857 (right panel). The individual Gaussian components are shown as blue dashed lines, while the overall fits to the absorption profiles are shown in solid red lines. The upper x-axis indicates the corresponding velocities relative to the emission redshifts of the foreground galaxies.

ranges from $7.0 \pm 1.3\,\mathrm{km\,s^{-1}}$ to $11.1 \pm 2.0\,\mathrm{km\,s^{-1}}$, with a median value of $9.3\,\mathrm{km\,s^{-1}}$. The width of absorption lines can serve as a constraint on the temperature of the absorbing gas, assuming that thermal motions are the primary driver of line broadening. However, this estimate represents an upper limit, as additional factors such as turbulence can also contribute to the observed broadening. Assuming a representative $\Delta v_{\mathrm{FWHM}} = 10\,\mathrm{km\,s^{-1}}$ for GOTOQs, we derive an upper limit on the kinetic temperature of the gas as $T_k \leqslant 2185$ K (S. Borthakur et al. 2010). This is higher than the T_s constraint we have obtained using the correlation between $E(B-V)$ and $\int \tau dv$ (see Section 4.3). This implies either the presence of nonthermal motions and/or hidden narrow components, which can be resolved by obtaining spectra at higher resolution and signal-to-noise ratio.

The integrated H I 21 cm optical depths are provided in column (4) of Table 2. The observed integrated H I 21 cm optical depths are consistent with these sightlines being DLAs (i.e., $\log[N_{\mathrm{H\,I}}/\mathrm{cm^{-2}}] \geqslant 20.3$) assuming a spin temperature of the gas, $T_s = 100$ K, and a covering factor (i.e., f_c[4]) of unity. This is in line with the finding of V. P. Kulkarni et al. (2022) that GOTOQs produce DLA (or sub-DLA; i.e., $19 \leqslant \log[N_{\mathrm{H\,I}}/\mathrm{cm^{-2}}] < 20.3$) in the ultraviolet spectra of the background quasars. The properties of the GOTOQs analyzed in this work and those compiled from the literature are summarized in Table 2.

In total, 9 of the 10 GOTOQs show detection of H I 21 cm absorption. The weakest H I 21 cm absorption was observed toward J1042+0748 with a measured $\int \tau dv$ of $0.19\,\mathrm{km\,s^{-1}}$ (S. Borthakur et al. 2010). If we consider the limiting $\int \tau dv$ of $0.3\,\mathrm{km\,s^{-1}}$ as typically considered in the literature (e.g., R. Dutta et al. 2017c), then the H I 21 cm detection rate is ∼80% for GOTOQs. This is by far the largest detection rate for H I 21 cm absorption in any population of isolated, intervening galaxies. Such large detection rates (i.e., ∼ 80%) are also seen toward galaxy mergers at similar redshifts (R. Dutta et al. 2018, 2019). The optical depth measured in the case of detections is consistent with them being DLAs (assuming $f_c = 1$ and $T_s = 100$ K), except for J1042+0748, where VLBI observations constrain the H I column density to $N_{\mathrm{H\,I}} \leqslant 1.5 \times 10^{20}\,\mathrm{cm^{-2}}$ (S. Borthakur et al. 2010).

To characterize the kinematic spread of the H I 21 cm absorbing gas, we estimate Δv_{90}, defined as the velocity range within which 90% of the total integrated optical depth is contained. The computed Δv_{90} values are listed in column (5) of Table 2. For the GOTOQs, Δv_{90} ranges from 4 to $52.8\,\mathrm{km\,s^{-1}}$, with a median value of $18.1\,\mathrm{km\,s^{-1}}$. This is consistent with the distribution of low-redshift ($z \leqslant 0.4$) H I 21 cm absorbers associated with DLAs, strong Fe II/Mg II metal absorbers, and QGPs. In the sample compiled by R. Dutta et al. (2017b), Δv_{90} ranges from 10 to $59\,\mathrm{km\,s^{-1}}$ (median $11\,\mathrm{km\,s^{-1}}$) for low-z DLAs, from 4.5 to $39\,\mathrm{km\,s^{-1}}$ (median 19.1 $\mathrm{km\,s^{-1}}$) for low-z strong Fe II/Mg II absorbers, and from 1.1 to $76\,\mathrm{km\,s^{-1}}$ (median 19.7 $\mathrm{km\,s^{-1}}$) for low-z QGPs. This is expected as GOTOQs are usually strong Fe II/Mg II absorbers (L. K. Guha & R. Srianand 2023, 2024) and are typically associated with DLAs or sub-DLAs (V. P. Kulkarni et al. 2022). However, note that, compared to the high-redshift ($z > 0.4$) H I 21 cm absorbers associated with Fe II/Mg II absorption or DLAs, low-redshift H I 21 cm absorbers have significantly less spread in the velocity space (R. Dutta et al. 2017b).

4.1. Integrated Optical Depth versus Impact Parameter

In this subsection, we examine the dependence of the integrated H I 21 cm optical depth around galaxies on the impact parameter. Among the three new detections reported here, the impact parameter is precisely measured only for J1451+0857, where the foreground galaxy is clearly visible in the DESI-LIS images. In the other two cases, the foreground galaxies are not detected in the DESI-LIS images, likely because they are at a very low impact parameter and outshone by the bright background quasars. Precise measurements of the impact parameters in such cases typically rely on triangulation methods (P. Noterdaeme et al. 2010; L. K. Guha & R. Srianand 2024). However, for now, we provide an upper limit on the impact parameters based on the fiber size, as the fiber captures nebular emission from the foreground galaxy, thereby constraining the maximum possible extent of the impact parameters. This is also the case for the GOTOQ J1443

[4] Covering factor is usually defined as the fraction of the background radio source occulted by the absorbing gas.

Table 2
Properties of the GOTOQs Studied in This Work

QSO	D (kpc)	z_{gal}	$\int \tau dv$ (km s^{-1})	Δv_{90} (km s^{-1})	12 + log(O/H)	$E(B-V)$	References
(1)	(2)	(3)	(4)	(5)	(6)	(7)	(8)
J075807.65+113646.0	<4.7	0.1870	1.64 ± 0.07	27.3	8.32	−0.071 ± 0.002	This work
J115948.76+582020.0	<3.8	0.2386	7.39 ± 0.04	11.9	8.52	+0.353 ± 0.007	This work
J145111.51+085757.8	8.0	0.1612	2.54 ± 0.28	8.4	8.70	+0.252 ± 0.007	This work
J011322.69+251853.3	6.0	0.2546	11.05	⋯	⋯	+0.597 ± 0.002	W. Hu et al. (2025)
J104257.58+074850.5	1.7	0.0332	0.19	4.0	8.42	+0.142 ± 0.004	S. Borthakur et al. (2010)
J124157.54+633241.6	11.1	0.1430	2.90 ± 0.16	52.8	8.7	+0.195 ± 0.002	N. Gupta et al. (2010)
J130028.53+283010.1	9.4	0.2229	⩽0.239	⋯	⋯	−0.089 ± 0.003	R. Dutta et al. (2017c)
J143806.79+175805.4	7.5	0.1468	4.89 ± 0.19	19.7	⋯	+0.060 ± 0.003	R. Dutta et al. (2017c)
J144304.53+021419.3	<5.1	0.3714	3.40 ± 0.10	16.5	8.4	+0.433 ± 0.002	N. Gupta et al. (2013)
J163956.35+112758.7	5.1	0.0790	15.70 ± 0.13	28.0	8.47	+1.112 ± 0.004	R. Srianand et al. (2013)

Note. Column (1) lists the coordinates of the background quasars, while columns (2) and (3) provide the impact parameters of the foreground galaxies and their emission redshifts, respectively. Column (4) presents the integrated H I 21 cm optical depth toward the background quasars associated with these galaxies. Column (5) represents 90% of the velocity width of the absorbing gas (Δv_{90}). Column (6) lists the gas phase metallicity of the foreground galaxies based on the nebular line ratios derived from the SDSS spectra. Column (7) indicates the line-of-sight reddening of the quasars caused by the foreground galaxies. Column (8) lists the references for the previously observed GOTOQs compiled in this study.

+0214 in the literature sample. To better investigate the dependence of the integrated optical depth on the impact parameter, we incorporate additional QGPs with $D \leqslant 40$ kpc previously studied by R. Dutta et al. (2017c). We consider only QGPs where the redshift of the background quasar is spectroscopically confirmed.

In the lower panel of Figure 3, we show the integrated H I 21 cm optical depth as a function of the impact parameter of galaxies. Blue points represent the GOTOQs, with those newly observed using uGMRT highlighted by square boxes. Green points indicate the QGPs studied by R. Dutta et al. (2017c), and orange points correspond to QGPs from the literature and compiled in R. Dutta et al. (2017c). Filled points denote H I 21 cm detections in absorption, whereas hollow points represent the 3σ upper limits on the integrated optical depth. In the upper panel of Figure 3, we show the normalized histogram of the impact parameter distribution for H I 21 cm detections (filled pink) and nondetections (black outline). It is apparent from this figure that the H I 21 cm absorption is detected predominantly in cases where the quasar line-of-sight passes through the immediate vicinity of the foreground galaxies. A Kendall τ rank correlation test, including the upper limits (G. C. Privon et al. 2020) between the impact parameter and the integrated H I 21 cm optical depth, yields a strong anticorrelation between the two with the rank correlation coefficient $\tau_r = -0.353$ and p-value of $\approx 9 \times 10^{-6}$ with the null hypothesis that they are not correlated. By including new samples of GOTOQs that probe small impact parameters, we confirm the anticorrelation between H I 21 cm optical depth and impact parameter reported in previous studies (S. J. Curran et al. 2016; R. Dutta et al. 2017c) at a much higher significance level. A Kolmogorov–Smirnov (KS) test comparing the impact parameter distributions of galaxies with H I 21 cm detections to those without shows that the underlying distributions are statistically very different (p-value of $\approx 3 \times 10^{-4}$, with the null hypothesis that two distributions are identical). Similarly, based on the KS test (p-value = 0.356), we find no significant redshift dependence in the detection of H I 21 cm absorption over the redshift range $0 < z < 0.4$.

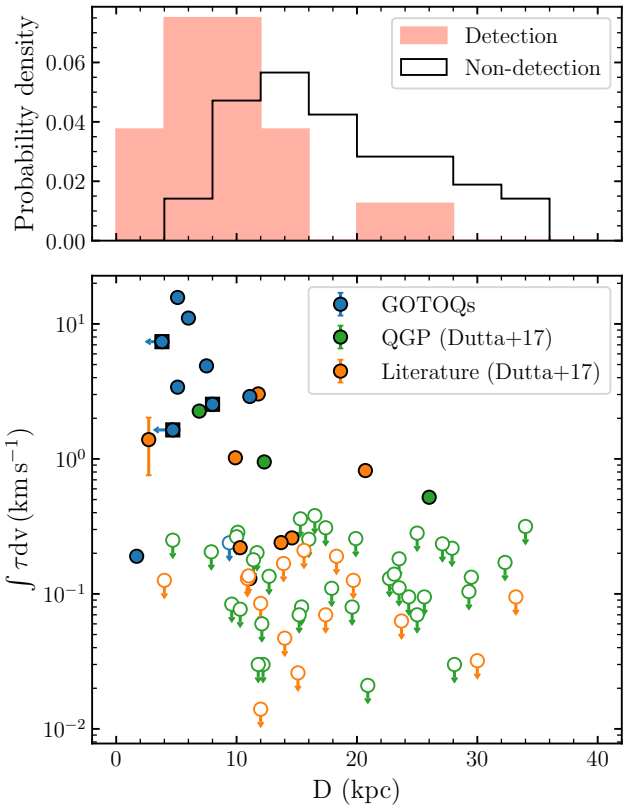

Figure 3. Lower panel: integrated H I 21 cm optical depth as a function of the impact parameter of galaxies. Blue points represent the GOTOQs, with newly observed GOTOQs using uGMRT highlighted by square boxes, while the remaining data points are taken from the literature. Green points indicate the quasar–galaxy pairs studied by R. Dutta et al. (2017c), and orange points correspond to quasar–galaxy pairs from the literature and compiled in R. Dutta et al. (2017c). Filled points denote H I 21 cm detections in absorption, whereas hollow points represent the 3σ upper limits on the integrated optical depth. Upper panel: normalized histogram of the impact parameter distribution for H I 21 cm detections and nondetections.

4.2. Detection Rate of Cold Neutral Gas around Galaxies

In this section, we examine the detection rate (C_{21}) of the cold H I gas, as traced by H I 21 cm absorption, around galaxies as a function of impact parameter (D). The detection

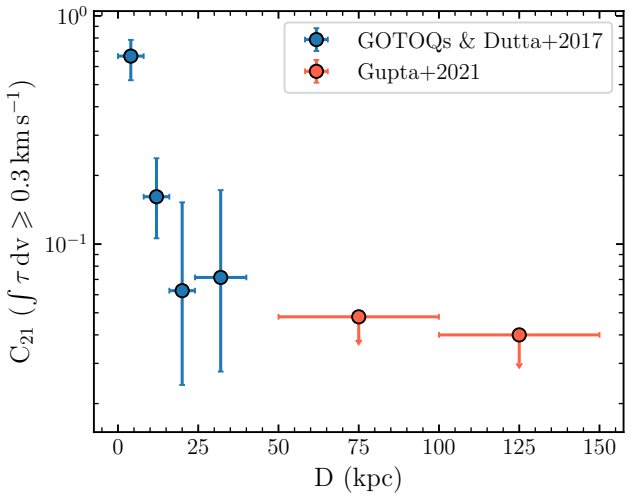

Figure 4. Covering fraction of H I 21 cm absorbers (C_{21}) as a function of impact parameter. Blue points show C_{21} across four impact parameter bins (0–8, 8–16, 16–24, and 24–40 kpc) for integrated optical depth sensitivities of 0.3 km s^{-1} for the GOTOQs and the QGPs studied and compiled from literature by R. Dutta et al. (2017c). Red points are taken from N. Gupta et al. (2021).

rate, C_{21}, is defined as the fraction of systems with H I 21 cm detections satisfying $\int \tau dv \geqslant 0.3$ km s^{-1}. Figure 4 shows C_{21} as a function of impact parameter bins (0–8, 8–16, 16–24, and 24–40 kpc) for the GOTOQs and QGPs studied and compiled from the literature by R. Dutta et al. (2017c). Additionally, red points from N. Gupta et al. (2021) represent C_{21} over larger impact parameter bins of 50–100 and 100–150 kpc. The error bars on C_{21} represent the 1σ Wilson binomial confidence intervals, while those on D reflect the bin size. The figure clearly shows a steep decline in C_{21} with increasing impact parameter as the measured C_{21} values are 67^{+12}_{-14}%, 16^{+8}_{-6}%, 6^{+9}_{-4}%, and 7^{+10}_{-4}% for the impact parameter bins of 0–8, 8–16, 16–24, and 24–40 kpc. There is no H I 21 cm absorption detected beyond this impact parameter, and upper limits on C_{21} of $\leqslant$0.048 and $\leqslant$0.040 over the impact parameter bins of 50–100 kpc and 100–150 kpc, respectively, were obtained by N. Gupta et al. (2021). A Kendall τ rank correlation test, including the upper limits (G. C. Privon et al. 2020), confirms an anticorrelation between C_{21} and D, with a rank correlation coefficient of $\tau_r = -0.814$ and a p-value of 0.021. To account for measurement uncertainties, we generated Monte Carlo realizations of the dataset. Symmetric errors on D were sampled uniformly over the bin, while asymmetric errors on C_{21} were represented using split-normal distributions. Upper limits in C_{21} were sampled uniformly between zero and the measured value. For each realization, the Spearman correlation coefficient and its p-value were computed. Repeating this process across 10,000 realizations produced distributions of correlation coefficients and p-values that incorporate both symmetric and asymmetric measurement uncertainties, enabling robust estimation of the correlation and its uncertainty. This resulted in the rank correlation coefficient of $r_s = -0.886^{+0.229}_{-0.057}$ and the p-value of $0.019^{+0.092}_{-0.014}$.

Note, C_{21} will depend upon the following factors: (i) covering factor of gas with N(H I) sufficiently high to produce H I 21 cm absorption, (ii) fraction of cold gas contributing to this N(H I), and (iii) structure of the background radio source. Independent measurement of N(H I) either through UV spectra along the quasar line of sight or through H I 21 cm emission, along with higher spatial resolution VLBI observations to resolve the structure of background radio sources, would be highly valuable for interpreting the results.

4.3. Line-of-sight Reddening, Integrated Optical Depth, and Spin Temperature

We estimate the line-of-sight reddening of the background quasar caused by foreground galaxies in the GOTOQs sample, assuming the gas follows an extinction curve similar to that of the Small Magellanic Cloud (SMC; K. D. Gordon et al. 2003). Note that for the rest frame wavelength range considered here, the choice of extinction curve has no significant effect on the below results. More robust measurements of reddening, including the actual extinction curve, can be obtained by including higher spatial resolution data that cover a wider range of wavelengths. To determine the line-of-sight reddening, we fitted the optical quasar spectra from SDSS using a standard quasar spectrum template (J. Selsing et al. 2016), redshifted to match the redshift of the background quasar. The SMC extinction curve was then applied at the redshift of the foreground galaxies, with the V-band extinction coefficient (A_V) as the sole free parameter, alongside a multiplicative scaling factor, following the method described by R. Srianand et al. (2008). Column (7) of Table 2 provides the color excess, $E(B-V)$, for the background quasars resulting from line-of-sight reddening (assuming $R_V = 2.74$). The resultant fits for the GOTOQs studied in this paper are shown in Appendix B. For the GOTOQs, $E(B-V)$ ranges from -0.089 to 1.112, with a median value of 0.223. Note that the negative value of $E(B-V)$ in some cases is the consequence of intrinsic variance of the quasar spectral energy distribution (SED). Further note that among the GOTOQs analyzed in this study, only J1451+0857 exhibits strong Mg II absorption ($W_{2796} = 0.72 \pm 0.10$ Å) at $z = 0.6633$. In the literature sample, J1241+6323 shows multiple Mg II and C IV absorbers along the line of sight, while J1438+1758 and J1443+0214 exhibit C IV absorption at $z = 1.7874$ and Mg II absorption at $z = 1.8024$, respectively. Given the difficulty in quantifying the individual contributions of these absorbers to the line-of-sight reddening, we assume that the GOTOQs are the dominant contributors, as the lines of sight intersect the disks of the foreground galaxies.

In Figure 5, we show the integrated optical depth of H I 21 cm absorption for the GOTOQs as a function of color excess, $E(B-V)$. The figure shows a strong correlation between the integrated optical depth and line-of-sight reddening. A Kendall τ rank correlation test between $E(B-V)$ and $\int \tau dv$ yields a positive correlation coefficient of $r_\tau = 0.669$ with the p-value of 0.007. We perform a linear fit between $E(B-V)$ and $\int \tau dv$ for the GOTOQs, incorporating upper limits, following the prescription described in L. K. Guha et al. (2022) and R. Dutta et al. (2020b). We define the likelihood function as the product of likelihoods for the detections and the nondetections, as follows:

$$\mathcal{L}(\Upsilon) = \left(\prod_{i=1}^{n} \frac{1}{\sqrt{2\pi\sigma_i^2}} \exp\left\{ -\frac{1}{2} \left[\frac{\Upsilon_i - \Upsilon(\mathcal{E}_i)}{\sigma_i} \right]^2 \right\} \right) \times \left(\prod_{i=1}^{m} \int_{-\infty}^{\Upsilon_i} \frac{d\Upsilon'}{\sqrt{2\pi\sigma_i^2}} \exp\left\{ -\frac{1}{2} \left[\frac{\Upsilon' - \Upsilon(\mathcal{E}_i)}{\sigma_i} \right]^2 \right\} \right),$$

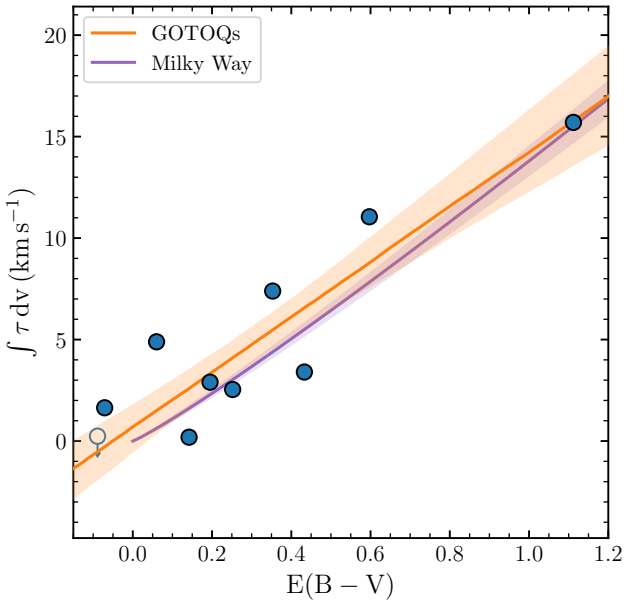

Figure 5. Integrated optical depth for H I 21 cm absorption in GOTOQs compared to the color excess, $E(B-V)$, caused by line-of-sight reddening. The occurrence of negative $E(B-V)$ values indicates possible systematic uncertainty of ∼0.1 mag due to the quasar-to-quasar SED variations. However realistic estimation of error in $E(B-V)$ will be achieved if we can use simultaneous SED measurements covering the rest UV-to-IR range. The solid orange line represents the best-fit relation, while the shaded region indicates the 1σ uncertainty in the fit. The purple line and the corresponding shaded region correspond to the best-fit relation taken from H. Liszt (2019) for the Milky Way H I 21 cm absorbers.

with $\Upsilon_i = \left(\int \tau\, dv\right)_i$, and $\mathcal{E}_i = E(B-V)_i$, corresponding to the ith measurement, whereas $\sigma_i = \sqrt{\sigma_{int}^2 + \sigma_{\Upsilon_i}^2}$ is defined so as to allow for the intrinsic scatter in the relation. The resulting best-fit relation is given by

$$\int \tau\, dv\ (\mathrm{km\ s^{-1}}) = 13.58^{+2.75}_{-2.35}\, E(B-V) + 0.68^{+1.06}_{-1.27}, \quad (1)$$

with an intrinsic scatter of $\sigma_{\rm int} = 2.69^{+0.84}_{-0.66}$ km s^{-1}. The solid orange line represents the best-fit relation, while the shaded region denotes the 1σ uncertainty. Interestingly, the best-fit relationship obtained is very much identical to the relationship obtained for the galactic sightlines by H. Liszt (2019), $\int \tau dv = (13.8 \pm 0.7) E(B-V)^{1.10\pm0.03}$ (see purple line in Figure 5), where $E(B-V)$ is derived using far-IR measurements. This likely indicates that the physical conditions prevailing in GOTOQ absorbers may be similar to what we see in the local ISM. Notably, in absorber-centric surveys, while stacked spectra of systems exhibiting H I 21 cm absorption along their line of sight tend to be significantly redder than those without, the correlation between integrated H I 21 cm optical depth and $E(B-V)$ for individual cases is not found to be statistically significant (R. Dutta et al. 2017b).

Using the standard relationship between N(H I) and $\int \tau dv$, we obtain $N(\mathrm{HI})[\mathrm{cm^{-2}}] \simeq 2.48^{+0.50}_{-0.43} \times 10^{19} \times \frac{T_s}{f_c} \times E(B-V)$. Here, T_s is the spin temperature in K, and f_c represents the gas covering factor of the background radio sources. For our discussion, we assume $f_c = 1$. Previous studies by K. D. Gordon et al. (2003) and S. B. Gudennavar et al. (2012) have established empirical relationships between N(H I) and $E(B-V)$ in the local Universe. Specifically, the proportionality constants are 3.05×10^{21}, 1.11×10^{22}, and 3.61×10^{22} for the Milky Way (S. B. Gudennavar et al. 2012), Large Magellanic Cloud (LMC), and SMC (K. D. Gordon et al. 2003), respectively. Based on these relations, we estimate the harmonic mean spin temperature (T_s) for gas along GOTOQ sightlines to be approximately 123, 448, and 1456 K, assuming dust properties similar to those of the Milky Way, LMC, and SMC, respectively. Comparing these results with direct measurements of N(H I) will not only provide further constraints on T_s but also help characterize the dust properties in GOTOQs.

Given that gas-to-dust ratios in galaxies strongly depend on gas-phase metallicity (A. Rémy-Ruyer et al. 2014), the metallicity of GOTOQs can provide additional constraints on the T_s when compared to those of the SMC, LMC, and Milky Way. For the three GOTOQs in our sample, we estimate the gas-phase metallicity using nebular line diagnostics, incorporating [O II], [O III], Hβ, and Hα emission lines. This analysis is performed with the publicly available PYTHON-IZI code (M. Mingozzi et al. 2020), utilizing the photoionization grid of E. M. Levesque et al. (2010). Since [N II] lines are not always detected in these cases, the derived metallicities exhibit a double-valued degeneracy. To ensure consistency, we adopt the upper-branch metallicities. The resulting values are listed in column (6) of Table 2. The metallicities of the GOTOQs reported in the literature are obtained from their respective sources. The median gas-phase metallicity of the GOTOQs in our sample is $12 + \log(\mathrm{O/H}) = 8.47$, corresponding to $\approx 0.6 Z_\odot$. This value is comparable to the metallicity of the LMC ($12 + \log(\mathrm{O/H}) = 8.5$; J. Roman-Duval et al. 2022), suggesting that the expected spin temperature in GOTOQs will be closer to the value we obtained from the Milky Way or LMC relationship between N(H I) and $E(B-V)$. However, we caution that the gas-phase metallicities derived from nebular emission lines in the star-forming region may not precisely match the metallicities along the quasar line of sight probing the cold neutral medium, as assumed in this analysis. Nonetheless, since the quasar sightlines for the GOTOQs pass through the star-forming disks, any discrepancies are likely to be minimal.

Lastly, we also measured $E(B-V)$ using SED fitting for the GOTOQ lines of sight with N(H I) measurements from UV spectroscopy obtained by V. P. Kulkarni et al. (2022). We do not find a significant correlation (Kendall τ rank correlation coefficient, $\tau_r = 0.25$ with p-value of 0.38) between N(H I) and $E(B-V)$ for this sample. This lack of correlation could be because of a few reasons: (i) small sample size (i.e., eight measurements); (ii) bias against reddened lines of sight in order to facilitate UV spectroscopy; and (iii) contribution to the H I column density from neutral gas components other than that probed by the H I 21 cm absorption, which is more sensitive to the colder neutral gas. It will be interesting to increase the number of N(H I) measurements for GOTOQs using UV spectroscopy in the future to check whether a tight correlation exists between N(H I) and $E(B-V)$. Finally, we point out that similar results were also found for high-z C I-selected DLAs by C. Ledoux et al. (2015).

5. Discussions and Conclusions

In this study, we have presented the results of our uGMRT search for intervening H I 21 cm absorption associated with GOTOQs. Our key results are summarized below.

Detection rate. We report three new detections of intervening H I 21 cm absorption at $z < 0.4$ associated with GOTOQs. This yields a 100% detection rate. When combining our results with previously studied GOTOQs in the literature, we find that H I 21 cm absorption is detected in 9 out of 10 GOTOQs at $z < 0.4$, corresponding to a detection rate of ≈90% (≈80% if we use $\int \tau dv$ sensitivity limit of 0.3 km s^{-1}). On the other hand, if we consider all the QGPs within an impact parameter of 8 kpc, we find the detection rate to be ≈67%. Nondetections at low impact parameters are predominantly around low surface brightness galaxies, where the H I content and extent may be less. When it comes to absorption-centric searches, the detection rate in the case of $z < 1$ DLAs (with impact parameters up to 45 kpc) is ≈61% (see Table 5 of R. Dutta et al. 2017c). The detection rate of H I 21 cm absorption from strong Mg II absorbers is ≈18%, where additional constraints on Fe II equivalent width can make the detection rate go up to ≈50% (R. Dutta et al. 2017a; R. Dutta et al. 2017b). Therefore, the highest detection rate of intervening H I 21 cm absorption is in the sample of GOTOQs, which can be attributed to the low impact parameter probed around star-forming galaxies ensured by the selection method itself.

Impact parameter dependence of the optical depth and detection rate. By combining our data with the existing literature, we find that both the velocity-integrated optical depth and the detection rate of H I 21 cm absorption decline rapidly with increasing impact parameter. The low detection rate of H I 21 cm absorption at high impact parameters could explain the low detection rate of H I 21 cm absorption in ongoing large surveys using MeerKAT and ASKAP. On the other hand, in the case of low-z DLAs showing H I 21 cm absorption, the associated galaxies are identified even up to 45 kpc. Note that DLA samples usually probe relatively higher redshifts compared to the QGPs. Therefore, differences in the impact parameter distribution could arise from (i) possible redshift dependencies, (ii) some of the DLAs originating from galaxies undergoing interactions that increase the H I cross section, and (iii) the identified nearby bright galaxies not being the actual host galaxies of the DLAs. Therefore, detailed host galaxy studies of absorber-centric H I 21 cm detections using integral field spectroscopic studies will provide important clues to understand the cross section of cold H I gas around galaxies.

Dust reddening and H I 21 cm optical depth. We identify a strong correlation between the line-of-sight reddening due to dust and the velocity-integrated optical depth of H I 21 cm absorption in GOTOQs. Interestingly, the observed correlation is very similar to the known relationship of the Milky Way. Confirming this trend with a larger sample of GOTOQs will be interesting. Further, it will be interesting to check whether these absorbers also follow a strong correlation between $E(B-V)$ and N(H I). However, in almost all the GOTOQs studied here, the background quasar is not bright enough in UV to measure N(H I). V. P. Kulkarni et al. (2022) have measured N(H I) toward a handful of GOTOQs. These sources do not show a strong trend between N(H I) and $E(B-V)$. It is not clear whether the lack of correlation is because of selection bias, where one tends to pick less reddened lines of sight for UV spectroscopic observations. On the other hand, based on stacking of SDSS spectra in Mg II absorption-selected samples, quasars with H I 21 cm absorption detected toward them have been found to be redder on average (R. Dutta et al. 2017b).

Future perspective. In the near future, data releases from wide-field, fiber-based spectroscopic surveys such as DESI (DESI Collaboration et al. 2016), the 4 m Multi-Object Spectrograph Telescope (R. S. de Jong et al. 2019), and the William Herschel Telescope Enhanced Area Velocity Explorer (S. Jin et al. 2024) are expected to significantly expand the catalog of known GOTOQs. Notably, DESI alone is set to provide approximately 4 million optical quasar spectra—an increase of 5 times the number of quasars with optical spectra compared to SDSS. In the early data release from DESI, covering a mere 2% of the DESI sky and featuring around 90,000 quasar spectra, we have identified about 200 GOTOQs at $z \lesssim 1$ (L. K. Guha et al. 2025, in preparation). Consequently, it is expected that the final sample will comprise around 10,000 GOTOQs. Assuming a 1% incidence of radio-loud quasars ($f_{\rm peak} \geqslant 30$ mJy) among these as found in our parent sample of GOTOQs, we anticipate about 100 GOTOQs with radio-loud quasars in the background. We plan to carry out a systematic survey of H I 21 cm and OH 18 cm absorption from these GOTOQs using uGMRT, Very Large Array, and MeerKAT (for the southern hemisphere). This will substantially increase our ability to statistically map the cold neutral and molecular gas distribution around galaxies and study their redshift evolution, given the success of our pilot survey.

Acknowledgments

This work makes use of the following software and packages: CASA (J. P. McMullin et al. 2007), AOFLAGGER (A. R. Offringa et al. 2012), NUMPY (C. R. Harris et al. 2020), MATPLOTLIB (J. D. Hunter 2007), SCIPY (P. Virtanen et al. 2020), ASTROPY (Astropy Collaboration et al. 2018), DUST_EXTINCTION (K. Gordon 2024), and ULTRANEST (J. Buchner 2021).

Appendix A
Radio Morphology of the Background Quasars

Here in Figure 6, we show the radio contours obtained from the uGMRT 1.4 GHz observations overlaid on the DESI r-band images centered on background quasars of the GOTOQs. The centroids of the radio contours are well-aligned with the optical centroids of the background quasars.

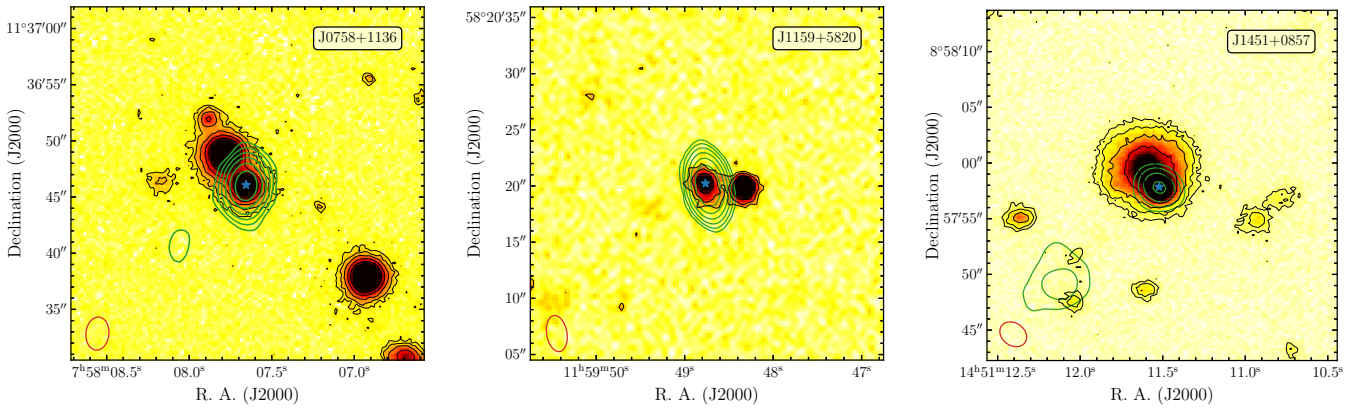

Figure 6. DESI-LIS *r*-band continuum images of the GOTOQs observed with the uGMRT. The green contours represent the radio continuum flux density from uGMRT observations with a 6.25 MHz bandwidth, centered on the expected H I 21 cm absorption frequency. The outermost green contour in each panel corresponds to 10σ above the median noise level, with successive inner contours increasing by factors of 2. The blue star marks the optical centroid of the background quasar. The black contours in each panel correspond to 3σ above the median noise level, with successive inner contours increasing by factors of 2. The uGMRT synthesized beam is shown with the red ellipse at the bottom-left corner in each panel.

Appendix B
Line-of-sight Reddening of the Background Quasars by the GOTOQs

Since the absorber rest-frame wavelengths do not extend below 3000 Å, the choice of extinction curve has little impact on the results. We obtain similar values of reduced χ^2 and $E(B-V)$ when using SMC, LMC, or Milky Way extinction curves. Therefore, we present the dust extinction fits for the GOTOQs studied in this work, assuming an SMC-like extinction curve (Figures 7, 8, and 9).

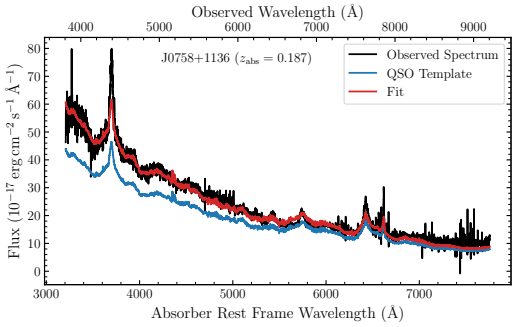

Figure 7. Estimation of the line-of-sight reddening of the background quasar caused by the foreground galaxy for the GOTOQ J0758+1136. The black spectrum is the observed spectrum of the background quasar, while the blue spectrum shows the template quasar spectrum redshifted to the redshift of the quasar. The red curve corresponds to the best-fit spectrum, obtained by applying a color excess of $E(B-V) = -0.071$ to the template spectrum at the redshift of the foreground galaxy. In this case, the quasar spectrum tends to be bluer than the template spectrum used. Such measurements are useful for quantifying the scatter in $E(B-V)$ propagating from the spread in the QSO SEDs.

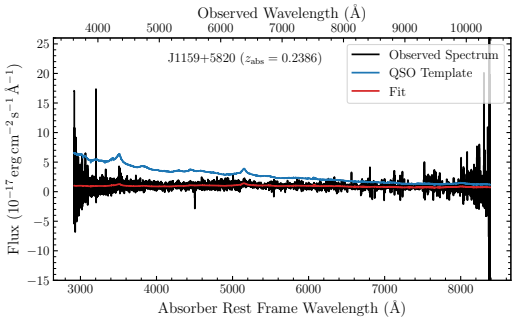

Figure 8. Same as the above figure, but for the GOTOQ J1159+5820.

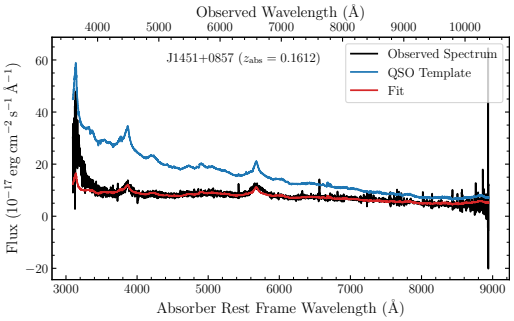

Figure 9. Same as the above figure, but for the GOTOQ J1451+0857.

ORCID iDs

Labanya K. Guha https://orcid.org/0009-0004-4263-077X
Raghunathan Srianand https://orcid.org/0000-0002-9062-1921
Rajeshwari Dutta https://orcid.org/0000-0002-6095-7627

References

Alam, S., Albareti, F. D., Allende Prieto, C., et al. 2015, ApJS, 219, 12
Allison, J. R., Sadler, E. M., Amaral, A. D., et al. 2022, PASA, 39, e010
Astropy Collaboration, Price-Whelan, A. M., Sipőcz, B. M., et al. 2018, AJ, 156, 123
Borthakur, S., Tripp, T. M., Yun, M. S., et al. 2010, ApJ, 713, 131
Borthakur, S., Tripp, T. M., Yun, M. S., et al. 2011, ApJ, 727, 52
Briggs, F. H., & Wolfe, A. M. 1983, ApJ, 268, 76
Buchner, J. 2021, JOSS, 6, 3001
Carilli, C. L., Menten, K. M., Reid, M. J., Rupen, M. P., & Yun, M. S. 1998, ApJ, 494, 175
Carilli, C. L., & van Gorkom, J. H. 1992, ApJ, 399, 373
Curran, S. J., Reeves, S. N., Allison, J. R., & Sadler, E. M. 2016, MNRAS, 459, 4136
Das, S., Joshi, R., Chaudhary, R., et al. 2025, A&A, 695, A207
de Jong, R. S., Agertz, O., Berbel, A. A., et al. 2019, Msngr, 175
DESI Collaboration, Aghamousa, A., Aguilar, J., et al. 2016, arXiv:1611.00036
Dey, A., Schlegel, D. J., Lang, D., et al. 2019, AJ, 157, 168
Ďurovčíková, D., Katz, H., Bosman, S. E. I., et al. 2020, MNRAS, 493, 4256
Dutta, R., Fumagalli, M., Fossati, M., et al. 2020b, MNRAS, 499, 5022
Dutta, R., Raghunathan, S., Gupta, N., & Joshi, R. 2020a, MNRAS, 491, 838
Dutta, R., Srianand, R., & Gupta, N. 2018, MNRAS, 480, 947
Dutta, R., Srianand, R., & Gupta, N. 2019, MNRAS, 489, 1099
Dutta, R., Srianand, R., Gupta, N., & Joshi, R. 2017a, MNRAS, 468, 1029
Dutta, R., Srianand, R., Gupta, N., et al. 2017b, MNRAS, 465, 4249
Dutta, R., Srianand, R., Gupta, N., et al. 2017c, MNRAS, 465, 588
Erb, D. K. 2008, ApJ, 674, 151
Field, G. B. 1959, ApJ, 129, 536

Gordon, K. 2024, JOSS, 9, 7023
Gordon, K. D., Clayton, G. C., Misselt, K. A., Landolt, A. U., & Wolff, M. J. 2003, ApJ, 594, 279
Gordon, Y. A., Boyce, M. M., O'Dea, C. P., et al. 2021, yCat, 255, 30
Gudennavar, S. B., Bubbly, S. G., Preethi, K., & Murthy, J. 2012, ApJS, 199, 8
Guha, L. K., & Srianand, R. 2023, MNRAS, 519, 3319
Guha, L. K., & Srianand, R. 2024, MNRAS, 532, 3056
Guha, L. K., Srianand, R., Dutta, R., et al. 2022, MNRAS, 513, 3836
Gupta, N. 2015, in SALT Science Conf. 2015 (SSC2015), ed. D. Buckley & A. Schroeder (Trieste: SISSA), 37
Gupta, N., Srianand, R., Bowen, D. V., York, D. G., & Wadadekar, Y. 2010, MNRAS, 408, 849
Gupta, N., Srianand, R., Noterdaeme, P., Petitjean, P., & Muzahid, S. 2013, A&A, 558, A84
Gupta, N., Srianand, R., Petitjean, P., Noterdaeme, P., & Saikia, D. J. 2009, MNRAS, 398, 201
Gupta, N., Srianand, R., Petitjean, P., et al. 2012, A&A, 544, A21
Gupta, N., Jagannathan, P., Srianand, R., et al. 2021, ApJ, 907, 11
Gupta, Y., Ajithkumar, B., Kale, H. S., et al. 2017, CSci, 113, 707
Harris, C. R., Millman, K. J., van der Walt, S. J., et al. 2020, Natur, 585, 357
Heiles, C., & Troland, T. H. 2003, ApJ, 586, 1067
Heiles, C., & Troland, T. H. 2004, ApJS, 151, 271
Hotan, A. W., Bunton, J. D., Chippendale, A. P., et al. 2021, PASA, 38, e009
Hu, W., Wang, Y., Li, Y., et al. 2025, ApJS, 277, 25
Hunter, J. D. 2007, CSE, 9, 90
Irwin, J. A. 1995, PASP, 107, 715
Jin, S., Trager, S. C., Dalton, G. B., et al. 2024, MNRAS, 530, 2688
Joshi, R., Srianand, R., Petitjean, P., & Noterdaeme, P. 2017, MNRAS, 471, 1910
Joshi, R., Srianand, R., Petitjean, P., & Noterdaeme, P. 2018, MNRAS, 476, 210
Kanekar, N., Prochaska, J. X., Ellison, S. L., & Chengalur, J. N. 2009, MNRAS, 396, 385
Kennicutt, R. C., & Evans, N. J. 2012, ARA&A, 50, 531
Kulkarni, V. P., Bowen, D. V., Straka, L. A., et al. 2022, ApJ, 929, 150
Ledoux, C., Noterdaeme, P., Petitjean, P., & Srianand, R. 2015, A&A, 580, A8
Levesque, E. M., Kewley, L. J., & Larson, K. L. 2010, AJ, 139, 712
Liszt, H. 2001, A&A, 371, 698
Liszt, H. 2019, ApJ, 881, 29
McMullin, J. P., Waters, B., Schiebel, D., Young, W., & Golap, K. 2007, in ASP Conf. Ser. 376, Astronomical Data Analysis Software and Systems XVI, ed. R. A. Shaw, F. Hill, & D. J. Bell (San Francisco, CA: ASP), 127
Mingozzi, M., Belfiore, F., Cresci, G., et al. 2020, A&A, 636, A42
Noterdaeme, P., Srianand, R., & Mohan, V. 2010, MNRAS, 403, 906
Offringa, A. R., van de Gronde, J. J., & Roerdink, J. B. T. M. 2012, A&A, 539, A95
Péroux, C., Nelson, D., van de Voort, F., et al. 2020, MNRAS, 499, 2462
Privon, G. C., Ricci, C., Aalto, S., et al. 2020, ApJ, 893, 149
Reeves, S. N., Sadler, E. M., Allison, J. R., et al. 2015, MNRAS, 450, 926
Reeves, S. N., Sadler, E. M., Allison, J. R., et al. 2016, MNRAS, 457, 2613
Rémy-Ruyer, A., Madden, S. C., Galliano, F., et al. 2014, A&A, 563, A31
Roman-Duval, J., Jenkins, E. B., Tchernyshyov, K., et al. 2022, ApJ, 928, 90
Roy, N., Chengalur, J. N., & Srianand, R. 2006, MNRAS, 365, L1
Rubin, K. H. R., Juarez, C., Cooksey, K. L., et al. 2022, ApJ, 936, 171
Sadler, E. M., Moss, V. A., Allison, J. R., et al. 2020, MNRAS, 499, 4293
Selsing, J., Fynbo, J. P. U., Christensen, L., & Krogager, J. K. 2016, A&A, 585, A87
Srianand, R., Gupta, N., Petitjean, P., Noterdaeme, P., & Saikia, D. J. 2008, MNRAS, 391, L69
Srianand, R., Gupta, N., Rahmani, H., et al. 2013, MNRAS, 428, 2198
Straka, L. A., Noterdaeme, P., Srianand, R., et al. 2015, MNRAS, 447, 3856
Straka, L. A., Whichard, Z. L., Kulkarni, V. P., et al. 2013, MNRAS, 436, 3200
Tumlinson, J., Thom, C., Werk, J. K., et al. 2013, ApJ, 777, 59
Virtanen, P., Gommers, R., Oliphant, T. E., et al. 2020, NatMe, 17, 261
White, R. L., Becker, R. H., Helfand, D. J., & Gregg, M. D. 1997, ApJ, 475, 479
York, D. G., Adelman, J., Anderson, John, E. J., et al. 2000, AJ, 120, 1579
York, D. G., Straka, L. A., Bishof, M., et al. 2012, MNRAS, 423, 3692
Zwaan, M. A., Liske, J., Péroux, C., et al. 2015, MNRAS, 453, 1268
Zwaan, M. A., van der Hulst, J. M., Briggs, F. H., Verheijen, M. A. W., & Ryan-Weber, E. V. 2005, MNRAS, 364, 1467